Check for updates

Unraveling the site-specific energy transfer driven tunable emission characteristics of Eu^{3+} & Tb^{3+} co-doped $Ca_{10}(PO_4)_6F_2$ phosphors†

Nimai Pathak, [iD] *[a] Bhagyalaxmi Chundawat,[b] Pratik Das, [iD] [c] Pampa Modak[d] and Brindaban Modak [iD] [ef]

In this study we have explored $Ca_{10}(PO_4)_6F_2$ as host to develop a variety of phosphor materials with tunable emission and lifetime characteristics based on Eu^{3+} and Tb^{3+} as co-dopant ions and the energy transfer process involved with them. The energy transfer from the excited state of Tb^{3+} ion to the $^5D_0$ state of Eu^{3+} makes it possible to tune the colour characteristics from yellow to orange to red. Further, such energy transfer process is highly dependent on the concentration of Eu^{3+} and Tb^{3+} ions and their site-selective distribution among the two different Ca-sites (CaO_9 and CaO_6F) available. We have carried out DFT based theoretical calculation for both Eu^{3+} and Tb^{3+} ions in order to understand their distribution. It was observed that in cases of co-doped sample, Tb^{3+} ions prefer to occupy the Ca2 site in the CaO_6F network while Eu^{3+} ions prefer Ca1 site in the CaO_9 network. This distribution has significant impact on the lifetime values and the energy transfer process as observed in the experimental photoluminescence lifetime values. We have observed that for the 1st series of compounds, wherein the concentration Tb^{3+} ions are fixed, the energy transfer from Tb^{3+} ion at Ca2 site to Eu^{3+} ion at Ca1 site is dominating (Tb^{3+}@Ca2 → Eu^{3+}@Ca1). However, for the 2nd series of compounds, wherein the concentration Eu^{3+} ions are fixed, the energy transfer process was found to occur from the excited Tb^{3+} ion at Ca1 site to Eu^{3+} ions at both Ca1 and Ca2 (Tb^{3+}@Ca1 → Eu^{3+}@Ca1 and Tb^{3+}@Ca1 → Eu^{3+}@Ca2). This is the first reports of its kind on site-specific energy transfer driven colour tunable emission characteristics in Eu^{3+} and Tb^{3+} co-doped $Ca_{10}(PO_4)_6F_2$ phosphor and it will pave the way for the future development of effective colour tunable phosphor materials based on a single host and same co-dopant ions.

1 Introduction

White light-emitting diodes (WLEDs), a new generation solid-state lighting system, are dominating today's lighting industry. WLEDs are environmentally benign in nature, long-lasting and offer significant energy savings compared to the earlier fluorescent or incandescent lamps, which are now being replaced by WLEDs worldwide.[1–3] Most of the current commercial WLEDs are phosphor-converted (pc-WLEDs) using a combination of a blue LED chip and the yellow phosphor $(Y_3Al_5O_{12}:Ce^{3+})$. However, the lack of a red light emitting component makes the color-rendering index (CRI) lowers than 80.[4] An alternative approach is to use an ultraviolet (UV) or near-UV LED chip combined with blue, green, and red phosphors, which may generate warm white light with high CRI value after a proper adjustment of the ratio of tricolour phosphors. In such cases it is desirable that all the three phosphors have similar thermal and chemical stability and a degradation of colour of any of the three phosphors will change the ratio of three colours and result in different light instead of white light. The crystal lattice of such host matrix should not degrade and there should not be any chemical reaction on the surface due to exposure to outer atmosphere. One of the best ways to overcome such problem is to develop blue, red and green phosphors based on the same host matrix and using similar activators (such as rare earth ion), which have high thermal and chemical stability. Therefore, development of colour tunable phosphor materials based on same host and dopant ion's composition would be a promising area of research work in the field of light emitting materials.

[a] *Radiochemistry Division, Bhabha Atomic Research Centre, Mumbai, 400085, India. E-mail: nmpathak4@gmail.com; nimai@barc.gov.in; Fax: +91-22-25405151; Tel: +91-22-25590715*

[b] *Ex MSc Student from KJ Somaiya College of Science & Commerce, Vidyavihar, Mumbai, India*

[c] *Fuel Chemistry Division, Bhabha Atomic Research Centre, Mumbai, 400085, India*

[d] *Radiological Safety Division, Atomic Energy Regulatory Board, Anushaktinagar, Mumbai, 400094, India*

[e] *Theoretical Chemistry Section, Bhabha Atomic Research Centre, Mumbai-400 085, India*

[f] *Homi Bhabha National Institute (HBNI), Mumbai, India*

† Electronic supplementary information (ESI) available. See DOI: 10.1039/d1ra04941k

Apatite based host matrices with general formula of $M_{10}[TO_4]_6Z_2$, where M is the cationic site with +1, +2 or +3 charges (*e.g.* K^+, Na^+, Ca^{2+}, Sr^{2+}, Ba^{2+}, Pb^{2+}, Mn^{2+}, La^{3+}, Y^{3+}, Ce^{3+} *etc.*), and $[TO_4]$ represents anion group (*e.g.* SiO_4^{4-}, PO_4^{3-}, GeO_4^{4-}, MnO_4^{4-}, VO_4^{3-}, AsO_4^{3-}, SO_4^{4-} *etc.*), and Z is anion with -1 or -2 charges (*e.g.* O^{2-}, OH^- and halogen ions), possess high chemical and thermal stability and considered as an efficient host to develop a variety of phosphor materials with high luminescence efficiency.[5–7] Due to their high thermal, chemical and radiation stability such matrices are even potential candidate as host for immobilization of hazardous and highly radioactive nuclear waste.[8,9] Among them the fluorapatite based compounds with formula $M_{10}(PO_4)_6F_2$, (where M = Ca, Sr, Ba *etc.*) is advantageous owing to their abundance and high strength and thermal stability. As shown in Fig. 1, there are two different types of cationic sites in the crystal structure of $Ca_{10}(PO_4)_6F_2$, namely the nine-fold coordinated Ca1 site in the $[CaO_9]$ polyhedron with C_3 point symmetry and seven-fold coordinated Ca2 site in the $[CaO_6F]$ polyhedron with C_S point symmetry. Existence of these two different cationic sites have resulted in different emission characteristics of the same rare earth ion,[10] which indicates that for the development of colour tunable phosphor materials apatite based hosts are a favoured choice, wherein by changing the distribution of the rare earth ions one can generate a variety of colour.

Eu^{3+} and Tb^{3+} ions are the two widely used rare earth activators whose combined emissions covered a wide wavelength range in the blue-green-red region in the visible spectra. The $^5D_0 \rightarrow 7Fj$ ($j = 1, 2, 3$ & 4) transitions of Eu^{3+} ions results in emissions in the orange and red region *i.e.* 580–700 nm.[11] On the other hand Tb^{3+} ion has emission peaks around 540 nm and hence serves as a green center.[12] The blue emission of Tb^{3+} ion in the 370–450 nm range is generally quenched through the cross-relaxation between neighbouring Tb^{3+} ions.[13] However, owing to the efficient energy transfer from Tb^{3+} to Eu^{3+}, co-doping Eu^{3+} and Tb^{3+} ions is found to be a successful strategy to develop a variety of phosphor materials with not only tunable colour characteristics in the blue-green-red region but also with tunable lifetimes values just by varying their respective concentration while keeping the host lattice intact.[14–17]

In present case we have chosen $Ca_{10}(PO_4)_6F_2$ as host matrix to explore such tunable color characteristics. The two different Ca-sites (CaO_9 and CaO_6F) available for the dopant ions (Eu^{3+} and Tb^{3+} ion) makes it more flexible to tune the colour characteristics from yellow to orange to red. It has also been found that the F atom in the Ca-2 site made a significant difference in the lifetime and luminescence efficiency since F atom has less quenching effect compared to O atom.[8,9] Further, an energy transfer dynamics from Tb^{3+} ion to Eu^{3+} is associated with these compounds, which makes the tunable emission characteristics more exciting. Till date, no such study on site-specific energy transfer driven colour tunable emission characteristics in $Ca_{10}(PO_4)_6F_2$ is reported. Further, we have carried out density functional theory (DFT) based calculations in order to check the most favourable distribution of Eu^{3+} and Tb^{3+} ions among the two lattice sites available in $Ca_{10}(PO_4)_6F_2$ after considering a variety of possible substitutions. We have also considered the impact on any lattice ion vacancy on such distribution. We believe a comprehensive combined theoretical and experimental study on site-specific tunable colour characteristics and the associated lifetime values will pave the way for the future development of effective colour tunable phosphor materials based on a single host and same dopant ions.

2 Experimental

2.1. Synthesis of Eu^{3+} and Tb^{3+} co-doped $Ca_{10}(PO_4)_6F_2$ compounds

Precursor materials. Calcium carbonate ($CaCO_3$), europium oxide (Eu_2O_3), terbium oxide (Tb_2O_3), ammonium dihydrogen phosphate ($NH_4H_2PO_4$) and ammonium bi-fluoride (NH_4HF_2) were purchased from Sigma Aldrich and have been used for the compound preparation.

Synthesis procedure. Various Eu^{3+} and Tb^{3+} co-doped $Ca_{10}(PO_4)_6F_2$ compounds were synthesized by solid-state reaction method using appropriate amount of $CaCO_3$, Eu_2O_3, Tb_2O_3, $NH_4H_2PO_4$ and NH_4HF_2 following similar procedure as reported earlier.[8] These compounds were taken in appropriate amount and mixed in an agate mortar and the mixture was pelletized into a 10 mm diameter pellet. The pellets of various Eu^{3+} and Tb^{3+} co-doped compounds were then heated under high pure argon gas atmosphere in a stepwise manner at 500 K for 4 hours, 800 K for 4 hours and 1200 K for 14 hours without any interruption. After the final heat treatment, the solid product was collected and grind well and characterized by powder X-ray diffraction and FTIR spectroscopy. Various Tb^{3+} and Eu^{3+} doped samples such as 0.05 mol% Eu^{3+} and 0.5 mol% Tb^{3+} doped $Ca_{10}(PO_4)_6F_2$ (hereinafter $Eu_{0.05}$–$Tb_{0.5}$:CPF), 0.1 mol% Eu^{3+} and 0.5 mol% Tb^{3+} doped $Ca_{10}(PO_4)_6F_2$ (hereinafter $Eu_{0.1}$–$Tb_{0.5}$:CPF), 0.3 mol% Eu^{3+} and 0.5 mol% Tb^{3+} doped $Ca_{10}(PO_4)_6F_2$ (hereinafter $Eu_{0.3}$–$Tb_{0.5}$:CPF), 0.5 mol% Eu^{3+} and 0.5 mol% Tb^{3+} doped $Ca_{10}(PO_4)_6F_2$ (hereinafter $Eu_{0.5}$–$Tb_{0.5}$:CPF), 0.5 mol% Eu^{3+} and 0.05 mol% Tb^{3+} doped $Ca_{10}(PO_4)_6F_2$ (hereinafter $Eu_{0.5}$–$Tb_{0.05}$:CPF), 0.5 mol% Eu^{3+} and 0.1 mol% Tb^{3+} doped $Ca_{10}(PO_4)_6F_2$ (hereinafter $Eu_{0.5}$–
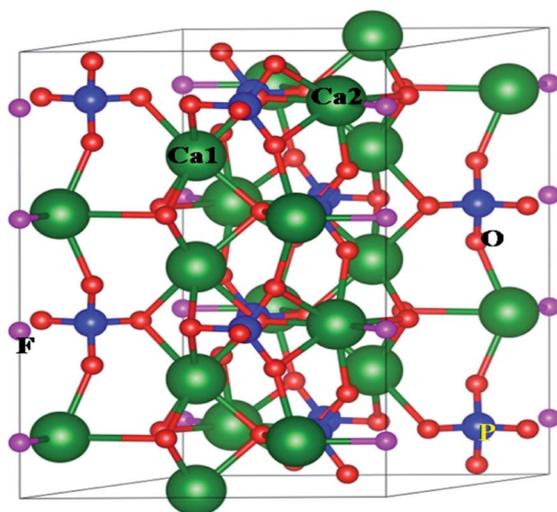

Fig. 1 $1 \times 1 \times 2$ supercell for $Ca_5(PO_4)_3F$ crystal structure.

Tb$_{0.1}$:CPF), 0.5 mol% Eu^{3+} and 0.3 mol% Tb^{3+} doped Ca$_{10}$(PO$_4$)$_6$F$_2$ (hereinafter Eu$_{0.5}$–Tb$_{0.3}$:CPF), were prepared using the solid state reaction method.

2.2. Instrumentation

The details of the instrumentation have been provided in ESI.†

2.3. Computational details

All the spin polarized density functional theory (DFT) calculations have been carried out employing the projector augmented wave (PAW) based electronic structure code Vienna *ab initio* simulation (VASP).[18,19] The set of valence states chosen in the present study for the pseudo potentials are Ca (3s^{2}3p^{6}4s^2), Eu (6s^{2}5p^{6}5d^1), Tb (6s^{2}5p^{6}5d^1), P (3s^{2}3p^2), F (2s^{2}2p^5) and O (2s^{2}2p^4). Perdew–Burke–Ernzerhof (PBE) functional within generalized gradient approximation (GGA) has been considered during the geometry optimization technique.[20,21] Full relaxation of both cell parameter and ionic positions for all the model structures has been considered during geometry optimization

process. The energy cut off for the expansion of electronic wave function has been kept fixed at 500 eV with self-consistent energy convergence of 10^{-6} eV throughout the calculations. Electronic structure calculations have been carried out using the optimized geometries. Monkhorst and Pack scheme has been adopted for generating Γ-centered k-point mesh during Brillouin zone sampling.[22] To overcome the limitations of conventional density functional theory we have used hybrid functional as prescribed by Heyd, Scuseria, and Ernzerhof (HSE06) during electronic structure calculations,[23] which has been shown to reproduce the experimental band gap of different semiconductor materials.[24] According to the HSE06 functional the exchange-correlation functional is defined by short-ranged (SR) and long-ranged (LR) parts of exchange. Short-ranged part is described by both Hartree–Fock (HF) exact exchange functional (E_X^{SR}) and PBE exchange functional ($E_X^{PBE,SR}$), while the long-ranged part is completely treated by PBE exchange functional ($E_X^{PBE,LR}$) as

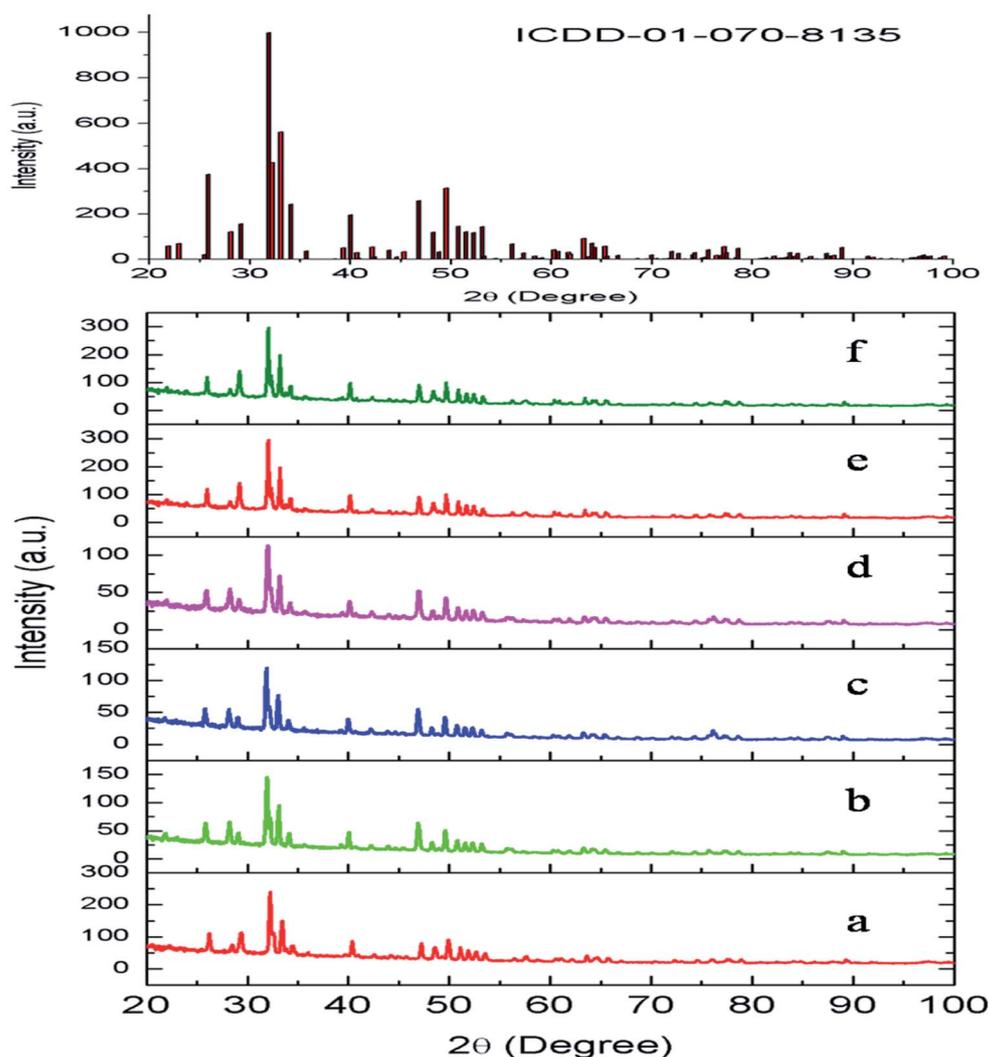$$E_{XC}^{HSE} = aE_X^{SR}(\mu) + (1-a)E_X^{PBE,SR}(\mu) + E_X^{PBE,LR}(\mu) + E_C^{PBE} \quad (1)$$

Fig. 2 XRD pattern of (a) Eu$_{0.3}$–Tb$_{0.5}$:CPF, (b) Eu$_{0.5}$–Tb$_{0.1}$:CPF, (c) Eu$_{0.5}$–Tb$_{0.3}$:CPF (d) Eu$_{0.5}$–Tb$_{0.05}$:CPF, (e) Eu$_{0.1}$–Tb$_{0.5}$:CPF, (f) Eu$_{0.5}$–Tb$_{0.5}$:CPF.

where, 'μ' indicates screening parameter, defines the distance of the short range interactions and 'a' is the HF mixing coefficient. The value of screening parameter and quantity of HF mixing are 0.2 Å^{-1} and 25%, respectively.

3   Results and discussion

3.1.   Phase purity and elemental analysis: X-ray diffraction (XRD) and X-ray fluorescence (XRF) study

The compounds obtained by solid-state reaction were characterized by X-ray diffraction technique. The obtained XRD of various Eu^{3+} and Tb^{3+} co-doped Ca$_{10}$(PO$_4$)$_6$F$_2$ compounds are shown in Fig. 2. All the compounds showed the characteristics XRD pattern of pure fluorapatite phase with ICDD file no. 01-070-8135. This has also confirmed that Eu^{3+} and Tb^{3+} ions were successfully substituted into lattice sites of calcium fluorapatite. The XRF spectra was recorded for Eu$_{0.1}$Tb$_{0.5}$:CPF and it is provided in the ESI,† which showed the peaks of Eu, Tb, Ca and P atoms at their respective energy position.

3.2.   Fourier-transform infrared (FTIR) spectroscopy study

IR spectrum of various compounds are shown in Fig. 3, which confirmed the existence of characteristics stretching and bending frequencies of phosphate groups of apatite. The transmission deep exist around 1075.81 cm^{-1}, 1024.17 cm^{-1}, 948 cm^{-1}, 589.5 cm^{-1} and 563 cm^{-1} are due to phosphate stretching vibration modes as reported earlier.[8]

3.3.   Geometry and electronic structure

At room temperature, Ca$_{10}$(PO$_4$)$_6$F$_2$ shows a hexagonal crystal structure (Fig. 1) with space group symmetry $P6_3/m$ (space group no. 176). Structural framework of Ca$_{10}$(PO$_4$)$_6$F$_2$ contains two different Ca lattice sites and three different O lattice sites whereas one type of lattice site for both P and F. The unit cell of Ca$_5$(PO$_4$)$_3$F contains two formula units (*i.e.*, 10 Ca, 6 P, 24 O, and 2 F). In can be noted that, the first type of Ca site (Ca1) is

coordinated by nine O atoms, while second type of Ca site (Ca2) is coordinated by six O atoms and one F atoms.[25] The calculated lattice parameter ($a = b = 9.495$ Å, and $c = 6.918$ Å) are found to be very close to the experimentally reported values ($a = b = 9.3783$ Å, and $c = 6.8888$ Å).[26–29] This justifies the choice of the computational methodology. To investigate the electronic structure of Ca$_5$(PO$_4$)$_3$F, we have analysed the density of states (DOS) and partial density of states (PDOS) (Fig. 4), which shows that the valence band maximum (VBM) is mainly composed of O 2p and F 2p states with small contribution of P (3p, 3s) and Ca (3p, 4s) states. On the other hand, the conduction band minimum (CBM) is dominated by P (3p, 3s) and F 2p states, with small contributions of Ca 4s state. The calculated band gap of Ca$_{10}$(PO$_4$)$_6$F$_2$ within HSE06 hybrid functional is found to be 7.26 eV, which is very close to the experimentally reported value of 7.21 eV for Ca$_5$(PO$_4$)$_3$F.[30]

Codoping of Eu^{3+} and Tb^{3+} in Ca$_{10}$(PO$_4$)$_6$F$_2$. To model (Eu, Tb)-codoped system, we have considered $1 \times 1 \times 2$ supercell for Ca$_{10}$(PO$_4$)$_6$F$_2$ which consist of total 84 atoms (20 Ca, 12 P, 48 O, and 4 F), and replaced two Ca by Eu and Tb. In this case, we have considered total six configurations (Str. 1–6 as shown in Fig. 5) by varying the lattice sites of dopant elements. For example, both Eu^{3+} and Tb^{3+} occupy lattice sites of Ca1 type in case of Str. 1 (Eu, and Tb at 1st neighboring lattice sites of each other) and Str. 2 (Eu, and Tb at 2nd neighboring lattice sites of each other). We have also calculated defect formation energies for various such structures of (Eu, Tb)-codoped Ca$_{10}$(PO$_4$)$_6$F$_2$ using the following relationship.[31,32]

$$\Delta H_f = E_{\text{doped}} - E_{\text{perfect}} + q\sum n_x \mu_x \qquad (2)$$

where, E_{doped} and E_{perfect} represent the energy of the codoped and pristine Ca$_{10}$(PO$_4$)$_6$F$_2$, calculated with same supercell size, μ_x stands for the chemical potential of the element X and n_x is

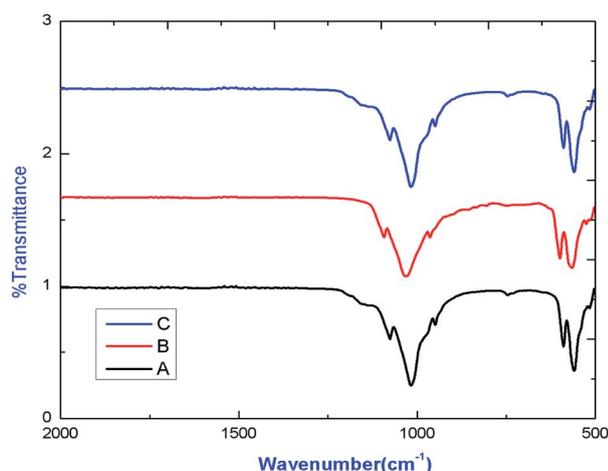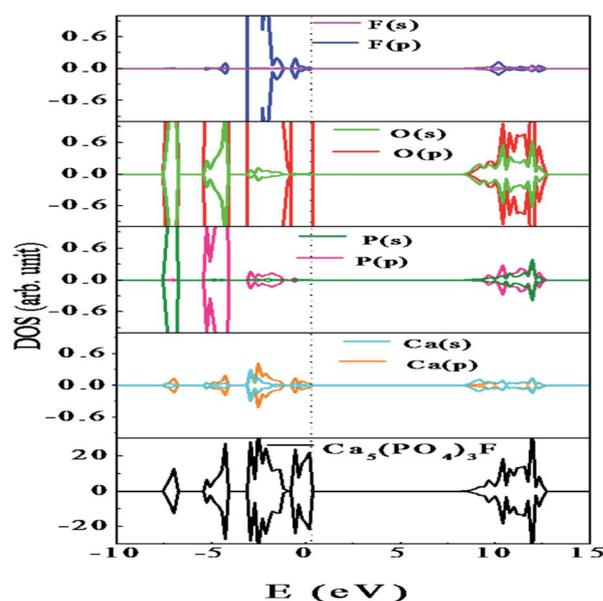**Fig. 3** FTIR spectra of (A) Eu$_{0.5}$–Tb$_{0.5}$:CPF, (B) Eu$_{0.5}$–Tb$_{0.3}$:CPF, (C) Eu$_{0.3}$–Tb$_{0.5}$:CPF.

Fig. 4 Density of states of Ca$_{10}$(PO$_4$)$_6$F$_2$. The vertical dashed line indicates the Fermi level.

the number of elements added ($q = -1$) or replaced ($q = +1$) to form the codoped system.

The formation energies of the various structures are given in Table 1. Lower the formation energy, higher the thermodynamic stability of the system. It should be noted that Str. 1 is energetically less stable by 0.24 eV in comparison to the Str. 2. On the other hand, both Eu, and Tb occupy lattice sites of Ca2 type in case of Str. 3 (Eu, and Tb at 1st neighboring lattice sites of each other) and Str. 4 (Eu, and Tb at 2nd neighboring lattice sites of each other). It is interesting to note that Str. 3, and Str. 4 are energetically more stable by 0.40 eV with respect to that of Str. 1. However, both types of configurations in this case are energetically comparable to each other. Finally we have

considered co-doping of Eu, and Tb involving both Ca1 and Ca2 types lattice sites, and generated two different structures viz. Str. 5 (Eu at Ca2 type site, while Tb at Ca1 type site) and Str. 6 (Eu at Ca1 type site, while Tb at Ca2 type site). Interestingly, Str. 5 and Str. 6 are energetically lower than the other four structures, and Str. 6 is found to be energetically most stable among all the possible structures considered in the present study. The calculated formation energy therefore follows the order, Str. 6 < Str. 5 < Str. 4 < Str. 3 < Str. 2 < Str. 1 while the stability of the structures follow the reverse order. This indicates that the Eu and Tb prefer different types of Ca lattice sites to form co-doped system. Since, both Eu and Tb normally exist in +3 states; there may be formation of Ca-vacancy in the co-doped system due to
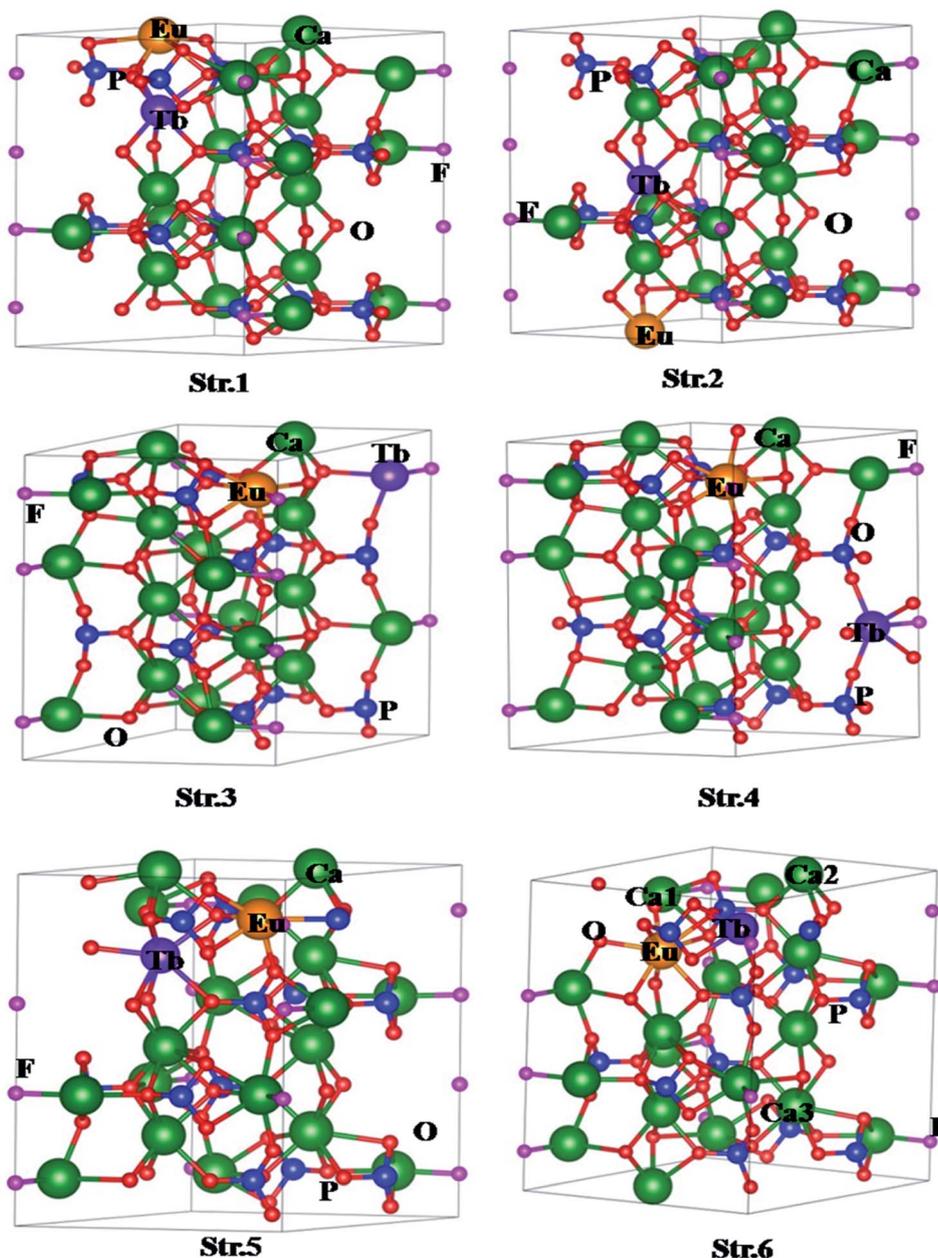

Fig. 5 Structures of for (Eu^{3+}, Tb^{3+}) co-doped $Ca_{10}(PO_4)_6F_2$ with different configurations. The numbers in Str. 6 denote positions of Ca vacancies.

Table 1 Calculated formation energies for the (Eu, Tb)-codoped $Ca_{10}(PO_4)_6F_2$ with different model structures and Ca vacancy defects

Systems	Structures	Formation energy (eV)
(Eu, Tb)-codoped $Ca_{10}(PO_4)_6F_2$	Str. 1	3.77
	Str. 2	3.53
	Str. 3	3.16
	Str. 4	3.15
	Str. 5	1.19
	Str. 6	1.10
(Eu, Tb)-codoped $Ca_{10}(PO_4)_6F_2$ with V_{Ca}	Str. 7	1.64
	Str. 8	2.64
	Str. 9	1.27

formation of charge compensated system. Therefore, we have also investigated the influence of Ca-vacancy on the electronic structure and properties of the codoped system. For this purpose, we have considered Str. 6, which is the lowest energy structure, and removed one Ca atom. In this case, we have considered three different structures by varying the position of Ca lattice site (indicated by Ca1, Ca2, Ca3 in Str. 6, Fig. 3). As for example, Str. 7 can be generated vacancy by removing Ca from the first neighbouring lattice of Eu (Ca1 in Str. 6, Fig. 3), Str. 8 from the second neighbouring lattice of both Eu and Tb (Ca3 in Str. 6, Fig. 3), and Str. 9 from the first neighbouring lattice of both Tb (Ca2 in Str. 6, Fig. 3). Interestingly, formation energy for Str. 7 has been found to be the lowest among the three (Table 1), indicating higher formation probability.

Electronic structure of (Eu^{3+}, Tb^{3+}) codoped $Ca_{10}(PO_4)_6F_2$ and (Eu, Tb)-codoped $Ca_{10}(PO_4)_6F_2$ in presence of Ca-vacancy. In this study, the electronic structure of Eu^{3+} & Tb^{3+} co-doped $Ca_{10}(PO_4)_6F_2$ system has been investigated by analysing the DOS and PDOS (Fig. 6a). We have considered lowest energy structure (Str. 6) for the electronic structure calculations. It has been observed that the doping of Eu^{3+} and Tb^{3+} at different type of Ca lattice sites results into introduction of discrete occupied impurity states at energy level 0.61 eV, 1.29 eV and 2.47 eV above the VBM. Analysis of PDOS indicates that the occupied impurity state is mainly composed by O (p) state with minor contribution of P (s, p), Eu (p, d) and Tb (p, d) states. Analysis of energy level indicates that the VBM and CBM levels are lowered by 0.03 eV and 0.14 eV, respectively compared to that of perfect $Ca_{10}(PO_4)_6F_2$. The Fermi energy is increased by 3.37 eV with respect to that $Ca_{10}(PO_4)_6F_2$. This is because of presence of excess electron in the (Eu, Tb)-codoped $Ca_{10}(PO_4)_6F_2$.

Interestingly, electronic structure for Eu^{3+} & Tb^{3+} co-doped $Ca_{10}(PO_4)_6F_2$ in presence of Ca-vacancy shows that the impurity states, as observed for (Eu, Tb)-codoped case, are completely disappear (Fig. 6b). This is due to the charge compensation system in presence of Ca-vacancy. Analysis of PDOS indicates that the VBM is mainly contributed by O (2p) states with minor contribution of F (2p) states, while the CBM is contributed by O (2s, 2p), P (3s, 3p), Eu (5d) and Tb (5d). Analysis of energy level indicates that the VBM is increased by 0.13 eV and CBM is decreased by 0.24 eV compared to that of perfect $Ca_{10}(PO_4)_6F_2$. The Fermi level is shifted towards the VBM by 2.28 eV with
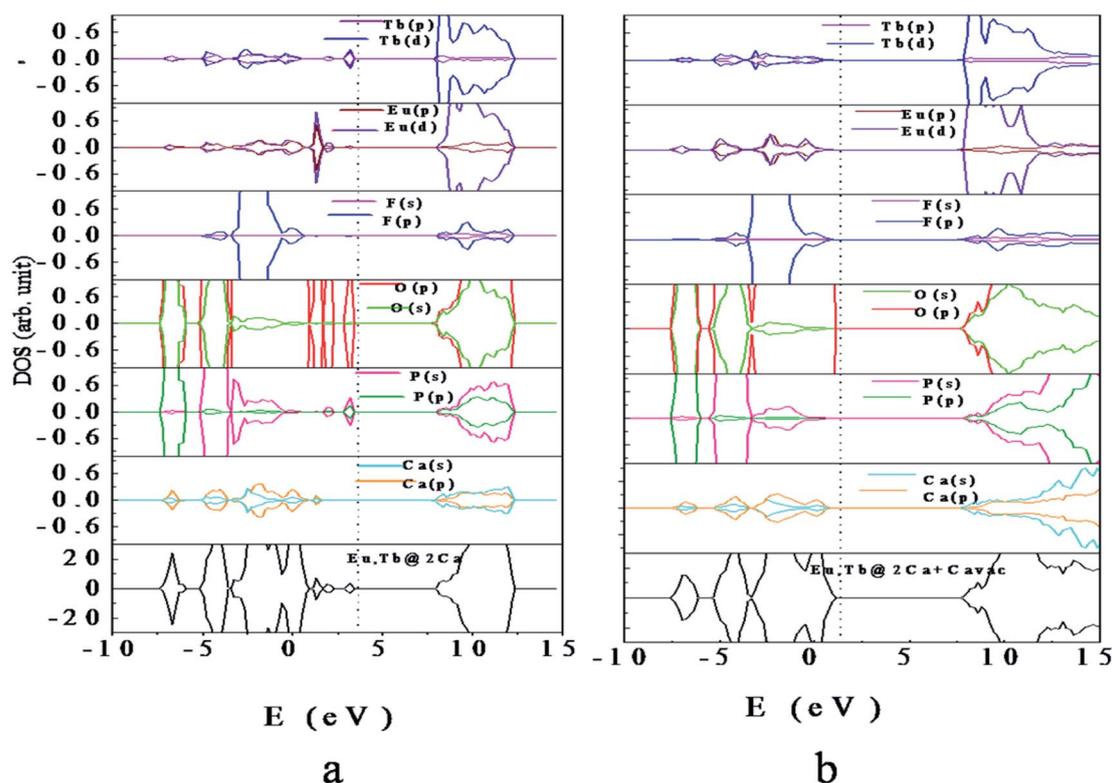
Fig. 6 Density of states of (a) Eu, Tb-codoped $Ca_{10}(PO_4)_6F_2$ (b) Eu, Tb-codoped $Ca_{10}(PO_4)_6F_2$ with Ca vacancy. The vertical dashed line indicates the Fermi level.

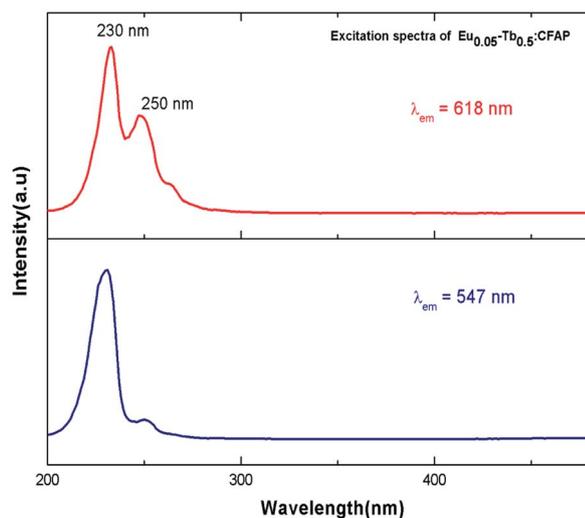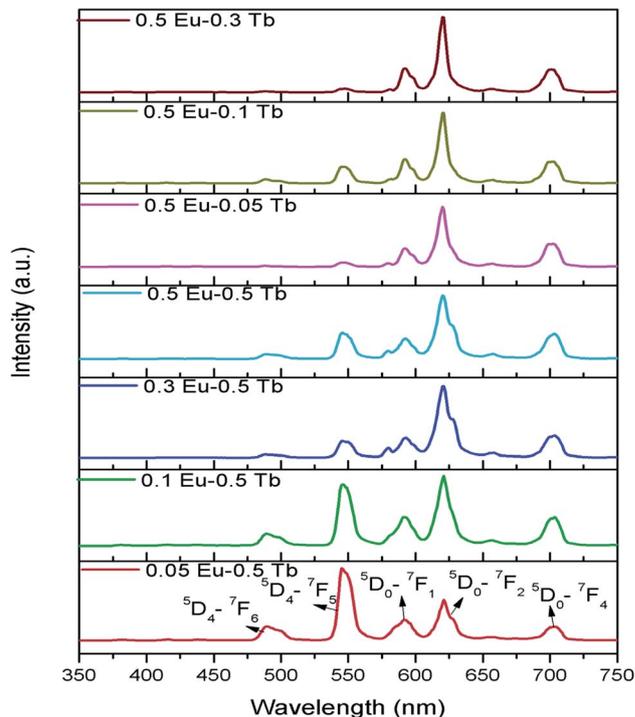Fig. 7 Excitation spectra of $Eu_{0.05}$–$Tb_{0.5}$:CFP at 618 nm and 547 nm emission wavelengths.

Fig. 8 Emission spectra of various mol% of Eu^{3+} and Tb^{3+} co-doped CFP compounds at 230 nm excitation wavelengths.

respect to that codoped system without Ca-vacancy. This is due to compensation of excess electron in presence of Ca-vacancy in the Eu^{3+} & Tb^{3+} co-doped $Ca_{10}(PO_4)_6F_2$.

3.4. Photoluminescence study

Fig. 7 represents the photoluminescence excitation spectra of $Eu_{0.05}$–$Tb_{0.5}$:CFP at 618 nm and 547 nm emission wavelengths. Two excitation bands peaking at 230 nm and 250 nm were observed for both the emission wavelengths, although their intensities are different. These transitions must be originate from the charge transfer transitions from 2p orbital of O^{2-} to the vacant 5d orbital of Tb^{3+} and Eu^{3+} respectively. Since the 547 nm emission wavelength is due to transition of $^5D_4 \rightarrow {}^7F_F$ of the Tb^{3+} ion,[33] the highly intense excitation peak at 230 nm can be attributed to the charge transfer transition from 2p orbital of O^{2-} to the vacant 5d orbital of Tb^{3+}. On the other hand at 618 nm emission wavelength, the peak intensity at 250 nm were found to be increased although 230 nm being the most intense one. The 250 nm excitation peak therefore can be attributed to the charge transfer transition from 2p orbital of O^{2-} to the vacant 5d orbital of Eu^{3+}.[34] The fact that even in case of 618 nm emission wavelength, the excitation peak at 230 nm (which is due to Tb^{3+} ion) is present in the PLE spectrum is suggesting that there might a possibility of energy transfer from Tb^{3+} ion to Eu^{3+} ion.

Fig. 8 represents the emission spectra of different Eu^{3+} and Tb^{3+} co-doped CFP compounds at 230 nm excitation wavelengths. The emission spectra consist of various emission peaks due to Eu^{3+} and Tb^{3+} ions. The emission peaks around 590, 618, and 704 nm are due to the $^5D_0 \rightarrow {}^7F_j$ ($j = 1, 2, 3$ and 4) transitions of Eu^{3+} ion[35] while the emission bands at 487, 547, 586 and 621 nm are due to Tb^{3+} ion's $^5D_4 \rightarrow {}^7J_j$ ($j = 6, 5, 4, 3$) transitions.[33] As it is known that for Eu^{3+} ion, the emission at 590 nm ($^5D_0$–$^7F_1$ transition) is a magnetic dipole (MD) transition while the red color emission around 618 nm ($^5D_0$–$^7F_2$ transition) and at 704 nm ($^5D_0$–$^7F_4$ transition) are electric dipole (ED)

transitions. The ED transition is hypersensitive to the local structure of Eu^{3+} ion and at an asymmetric environment, this transition is allowed one. The fact that ED transition's intensity is higher than the MD transition signifies that Eu^{3+} ion exists in an asymmetric environment.[34] For Tb^{3+} ion, the green emission at 547 nm i.e. $^5D_4$–$^7F_5$ is magnetic dipole (MD) transitions and not sensitive to local structure or crystal field strength. However, the blue emission i.e. $^5D_4$–$^7F_6$ transition around 487 nm is an electric dipole (ED) transitions, which is sensitive to the local environment although it is not hypersensitive.[33] We have calculated the respective color coordinates of various mol% of Eu^{3+} and Tb^{3+} co-doped CFP compounds at 230 nm excitation wavelengths as shown in Fig. 9. It can be seen that upon changing the concentration of any of the two dopant ion and keeping other dopant ion's concentration fixed, there is a change in color coordinated from yellow to orange to red. For the low dopant level of Eu^{3+} ion in $Eu_{0.05}$–$Tb_{0.5}$:CFP, the CIE color co-ordinates are placed in the yellow region while with increasing the concentration of Eu^{3+} ions, viz. in $Eu_{0.1}$–$Tb_{0.5}$:CFP and $Eu_{0.3}$–$Tb_{0.5}$:CFP, the color coordinates were shifted to orange and red regions. Similarly, by keeping the concentration of Eu^{3+} ion's fixed while varying the concentration of Tb^{3+} ions, the CIE color coordinates were found to be changed. It can be seen that with changing the concentration of Tb^{3+} ions viz. in $Eu_{0.5}$–$Tb_{0.1}$:CFP, $Eu_{0.5}$–$Tb_{0.2}$:CFP and $Eu_{0.5}$–$Tb_{0.3}$:CFP, the color can be tuned from orange to red. Therefore, a wide range of colored phosphors can be developed just by changing the relative concentration of Eu^{3+} and Tb^{3+} dopant ions.
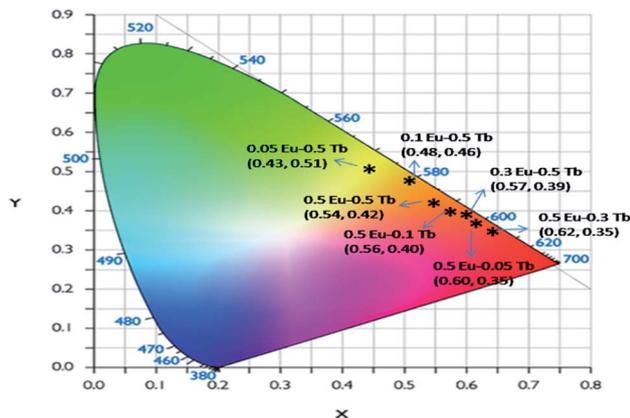
Fig. 9 CIE colour coordinates of various mol% of Eu^{3+} and Tb^{3+} co-doped CFP compounds at 230 nm excitation wavelengths.

Fig. 10a represents the emission spectra of different Eu^{3+} and Tb^{3+} co-doped CFP compounds at 250 nm excitation wavelengths, wherein we can see that the emission spectra for all the compounds are only consist of characteristics peaks of Eu^{3+} ions and that the peaks due to Tb^{3+} ions are very weak. This confirms that there is no charge transfer process involved at 250 nm excitation and that the 250 nm excitation peak is purely due to charge transfer transition from 2p orbital of O^{2-} to the vacant 5d orbital of Eu^{3+} ion.

It is worth mentioning here that these color tunable characteristics have been observed for 230 nm excitation wavelength only and for 250 nm excitation energy there is no such color tunable characteristics and all the compounds are red phosphor in nature as suggested by their calculated color coordinates represented in Fig. 10b. Therefore, the energy transfer dynamics from Tb^{3+} ion to Eu^{3+} ion at 230 nm excitation is solely responsible for such tunable color characteristics.[14–17] As shown

in Fig. 11, upon 230 nm excitation (which is due to CT transition from O^{2-} to the vacant 5d orbital of Tb^{3+} ion) many Tb^{3+} ions are excited to higher energy CT state from which it come back to the lower energy level $^5D_3$ and then to lower lying $^5D_4$ meta-stable state through non-radiative pathway. From $^5D_4$ level it is relaxed to lower energy levels through $^5D_4-^7F_{5,4,3}$ transitions. Few other Tb^{3+} ions at $^5D_3$ or $^5D_4$ levels transfer their energy to the $^5D_2$ level of Eu^{3+} ion which is known as the energy transfer. Now through a non-radiative decay from $^5D_2$ excited state the population of $^5D_0$ meta-stable state increases which results in emission through $^5D_0-^7F_J$ ($J = 0–6$) transitions.

The fact that with increasing the Tb^{3+} concentration there is an enhancement of Eu^{3+} ion's intensity while keeping it concentration unchanged as shown in Fig. 8, clearly indicates that there is a charge transfer process involved from Tb^{3+} ions to Eu^{3+} ion. Generally, the energy transfer from sensitizer (Tb^{3+}) to activator (Eu^{3+}) may takes place through either (i) the exchange interaction or (ii) electric multipolar transition. When the critical distance between the sensitizer and activator is shorter than 5 Å, then the energy transfer process use to take place via exchange interaction and when it is greater than 5 Å, the energy transfer from Tb^{3+} to Eu^{3+} ions happen in the way of electric multipolar interaction. The critical distance (R_c) between Tb^{3+} and Eu^{3+} can be calculated using eqn (3)[14,36]

$$R_c \approx \left[2 \frac{3V}{4X_c \pi Z} \right]^{1/3} \qquad (3)$$

where V is the volume of the unit cell, X_c is the critical dopant concentration, and Z is the number of host cations in the unit cell. For the $Ca_{10}(PO_4)_6F_2$, $X_c = 0.10$, $V = 534.35$ Å^3 and $Z = 2$, which gives a R_c value of 10.84 Å, which is larger than 5 Å. Therefore, energy transfer between Tb^{3+} and Eu^{3+} ions takes place due to electric multipolar interactions instead of exchange interaction.

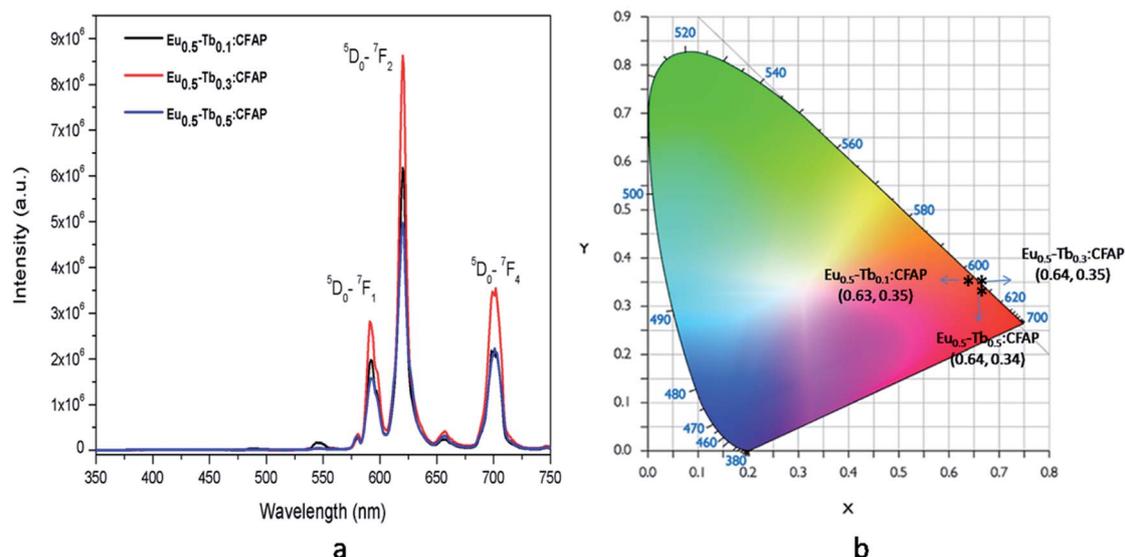**Fig. 10** Emission spectra of various mol% of Eu^{3+} and Tb^{3+} co-doped CFP compounds at 250 nm excitation wavelengths and their respective CIE colour coordinates.
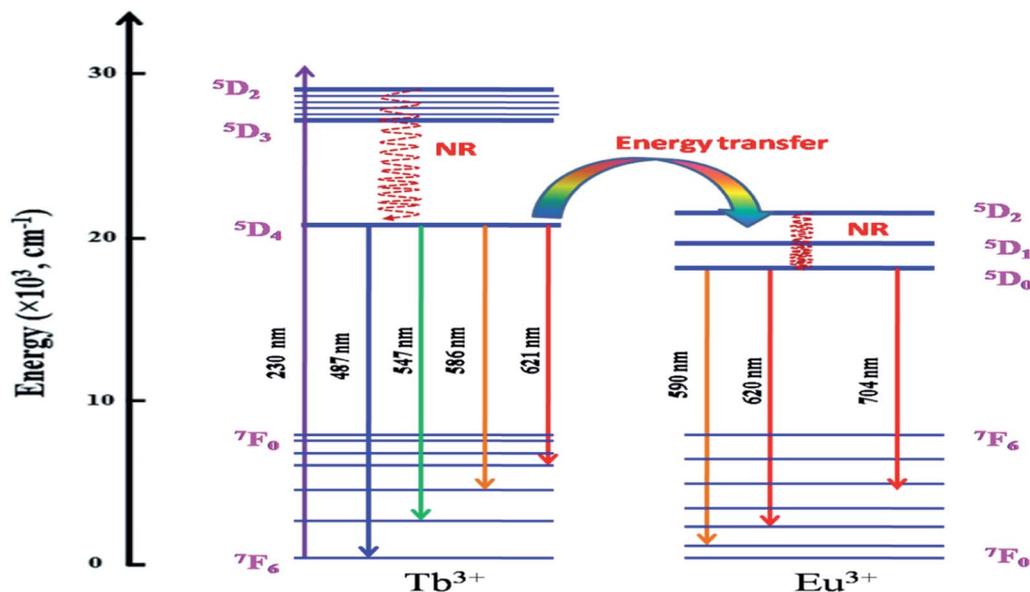
Fig. 11 Schematic energy level diagram of Tb^{3+} and Eu^{3+} and the energy transfer dynamics.

Now let us see how the lifetime of the respective excited states of the Tb^{3+} ions to Eu^{3+} ions behave while changing their concentration and the excitation energy. This will also provide information about the energy transfer mechanism.

3.5. Photoluminescence lifetime study

PL lifetime measurements can provide detail information regarding the energy transfer dynamics in addition to the lattice site occupancy of the dopant ions.[14–17] Since, there are two lattice sites (Ca1 and Ca2 sites) available for the dopant ions and as we have observed from DFT based calculation that the distribution of Eu^{3+} and Tb^{3+} among these two lattice sites are different, it will be interesting to see which sites are involved in the energy-transfer dynamics? The photoluminescence lifetime measurement has been carried out for all the compounds at 230 nm excitation wavelength (which is attributed to Tb^{3+} ions) and with emission wavelength 547 nm ($^5D_4$–$^7F_5$ transition of Tb^{3+} ion) and 618 nm ($^5D_0$–$^7F_2$ transition of Eu^{3+} ions) as shown in Fig. 12. We have observed that the decay profiles (both at 547 nm and 618 nm emission wavelength) for all the compounds followed a bi-exponential eqn (4).

$$I(t) = A_1 \exp\left(-\frac{t}{\tau_1}\right) + A_2 \exp\left(-\frac{t}{\tau_2}\right) \quad (4)$$

where $I(t)$ is intensity, τ_1 and τ_2 are emission decay times, and A_1 and A_2 are their relative weightage.

We have also calculated the percentage of a specific life-time using the formula in eqn (5)

$$\% \text{ of species } (n) = \left[\frac{(A_n \times \tau_n)}{\sum_n (A_n \times \tau_n)}\right] \times 100 \quad (5)$$

The lifetime values are included in Table 2 for all the compounds at different emission wavelength. As mentioned

before that due to the availability of two different Ca-sites (CaO_9 and CaO_6F); both Eu^{3+} and Tb^{3+} ions have a tendency to be distributed among the two lattice sites. Earlier, we have observed that the lifetime value for rare earth ion when placed at the Ca2 site (CaO_6F) which has an F-atom linkage, is more than when it is placed at Ca1 site (CaO_9). This is attributed to the F-atom, which has less quenching effect on the excited state and makes the lifetime value of the rare earth ions higher.[8,9] Therefore, the long lived component observed at 547 nm emission wavelength is due to Tb^{3+} ions present at Ca2 site while that at 618 nm emission is due to Eu^{3+} ions present at Ca2 site. On the other hand, the short-lived components for these two emission wavelength are due to Tb^{3+} and Eu^{3+} ions present at the Ca1 site, which has no F-atom linkage.

However, we have observed from our DFT calculation earlier that the stability of the Eu^{3+} and Tb^{3+} co-doped structure is more when Eu^{3+} ion is distributed at Ca1 site and Tb^{3+} ion at Ca2 site. The preference of distribution of Eu^{3+} ion is also reflected in the higher percentage of the short-lived component in many compounds viz. $Eu_{0.5}$–$Tb_{0.01}$:CFP, $Eu_{0.5}$–$Tb_{0.1}$:CFP, $Eu_{0.5}$–$Tb_{0.3}$:CFP, $Eu_{0.1}$–$Tb_{0.5}$:CFP. However, for Tb^{3+} ions such observation (higher percentage of the long-lived component) is not observed since the lifetime value of Tb^{3+} ions also depends on the energy transfer dynamics from Tb^{3+} ion to Eu^{3+} ion, which will decrease the percentage of contribution. The fact that there is an energy transfer process involved in this class of compounds can be explained based on decrease in lifetime value upon varying the concentration of Tb^{3+} ion or Eu^{3+} ion. Due to the energy transfer from the excited state of Tb^{3+} ion to the Eu^{3+} ion, the lifetime value of Tb^{3+} ion will be decreased, as observed earlier for various class of compounds.[14–17] The lifetime values of Eu^{3+} ion obtained for the Eu & Tb co-doped compounds in this work are found to be slight higher than that for pure Eu^{3+} doped CFP compounds reported earlier.[8] This might be due to the energy transfer process involved in the
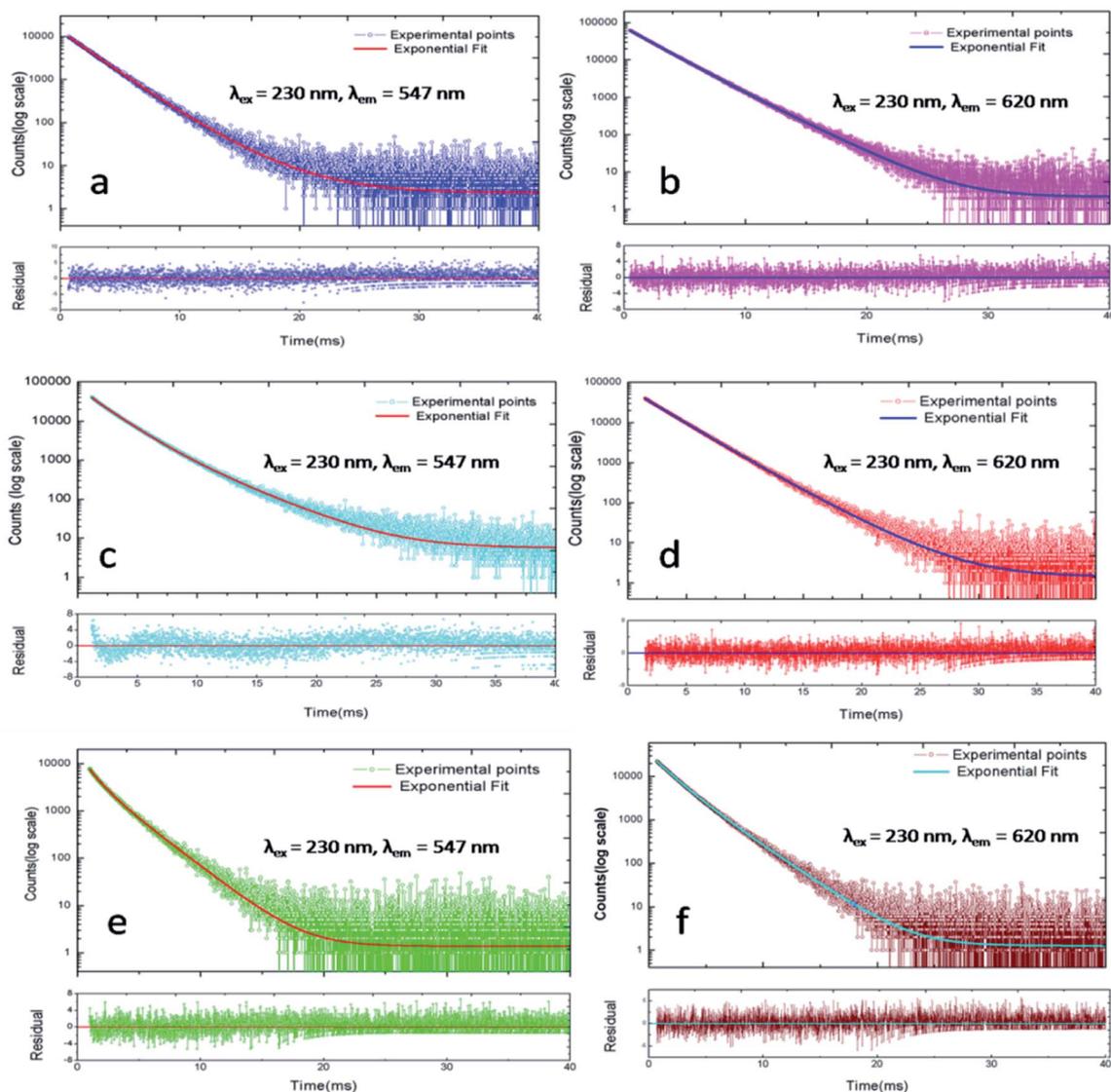
Fig. 12 Photoluminescence decay profile at $\lambda_{ex} = 230$ nm and $\lambda_{em} = 547$ nm & 620 nm for different Eu^{3+} and Tb^{3+} doped CFP compounds. (a and b) $Eu_{0.5}-Tb_{0.01}$:CFP; (c and d) $Eu_{0.5}-Tb_{0.1}$:CFP; (e and f) $Eu_{0.3}-Tb_{0.5}$:CFP (few spectra of other compounds are provided in the ESI†).

Table 2 PL lifetime values of Eu^{3+} and Tb^{3+} doped CFP compounds

Compound	PL lifetime components of Tb^{3+} ($\lambda_{ex} = 230$ nm and $\lambda_{em} = 547$ nm)		PL lifetime components of Eu^{3+} ($\lambda_{ex} = 230$ nm and $\lambda_{em} = 618$ nm)	
	Short-lived (τ_1) component in μs	Long-lived (τ_2) component in μs	Short-lived (τ_1) component in μs	Long-lived (τ_2) component in μs
$Eu_{0.5}-Tb_{0.01}$:CFP	2191.98 (90%)	4054.92 (10%)	2168.83 (59%)	2992.06 (41%)
$Eu_{0.5}-Tb_{0.1}$:CFP	1867.70 (70%)	3601.64 (30%)	2423.43 (89%)	3673.61 (11%)
$Eu_{0.5}-Tb_{0.3}$:CFP	1966.44 (86%)	3379.12 (14%)	2439.29 (93%)	3739.46 (7%)
$Eu_{0.1}-Tb_{0.5}$:CFP	1384.55 (35%)	2754.84 (65%)	2098.41 (67%)	3333.81 (33%)
$Eu_{0.3}-Tb_{0.5}$:CFP	952.79 (28%)	2203.12 (72%)	1477.1 (45%)	2527.96 (55%)
$Eu_{0.5}-Tb_{0.5}$:CFP	651.77 (24%)	2216.65 (76%)	1934.22 (45%)	2807.46 (55%)
$Na^+_2Eu^{3+}_2$:$Ca_6(PO_4)_6F_2$ (ref. 8)	—	—	1870 (23%)	2420 (77%)

present compounds. The fact that we have not seen a monotonic decrease or increase for few samples may be explained based on non-radiative pathways associated with various defect centers or vacancies, which also plays an important role in determining the lifetime of the excited state. These vacancies are generated due to the charge imbalance when Tb^{3+} or Eu^{3+} ions are substituted at a place of Ca^{2+} ion. The additional positive charge will lead to creation of negatively charged vacancies, which will have impact on the nearby Tb^{3+}/Eu^{3+} ion's local structure. Further, depending on the distance from the Tb^{3+}/Eu^{3+} ion, the impact will be different. We believe such vacancies are the main reason to not have any systematic decrease in the lifetime values for few samples.

Now let us consider two cases; (1) for the series of compounds where the concentration Eu^{3+} ion is fixed but that of Tb^{3+} ions is varied *viz.* for $Eu_{0.5}$–$Tb_{0.01}$:CFP, $Eu_{0.5}$–$Tb_{0.1}$:CFP and $Eu_{0.5}$–$Tb_{0.3}$:CFP compounds, and (2) for the series of compounds where the concentration Tb^{3+} ion is fixed but that of Eu^{3+} ions is varied *viz.* $Eu_{0.1}$–$Tb_{0.5}$:CFP, $Eu_{0.3}$–$Tb_{0.5}$:CFP and $Eu_{0.5}$–$Tb_{0.3}$:CFP. For the 1st series of compounds wherein the concentration of Tb^{3+} ion is varied, it is observed that the percentage of the long-lived Tb^{3+} component is small than its short-lived component. This is due to fact that the long-lived Tb^{3+} component at the Ca2 site mostly transfers its energy to nearby Eu^{3+} ions. Hence in this series, majority of the Tb^{3+} ions at Ca2 site are preferably taking part in the energy transfer dynamics and results in small contribution towards its radiative lifetime value and the radiation transition. Now for the second series of compound wherein the concentration of Tb^{3+} ion is fixed but that of Eu^{3+} ion is varied, the opposite thing has happened *i.e.* the percentage of the short-lived Tb^{3+} component is less than the long-lived component. Hence, we believe that for this series of compounds, majority of the Tb^{3+} ions at Ca1 site are preferably taking part in the energy-transfer process to Eu^{3+} ion. Now if we consider the lifetime values of Eu^{3+} ions, then for the 1st series compound the percentage of contribution of the short-lived Eu^{3+} component at Ca1 site is higher than that at Ca2 site. Further, with increasing the concentration of Tb^{3+} ion, the percentage of contribution of this short-lived component is found to increase. We have already concluded from DFT calculation that for Tb^{3+} and Eu^{3+} co-doped system, Eu^{3+} ions most preferably go to the Ca1 site and results in smaller lifetime value. Since there is no energy transfer process involved from the excited state of Eu^{3+} ions to other co-dopant ion, this percentage of contribution is linked to the contribution from Eu^{3+} ions at Ca1 and Ca2 sites to the overall red light emission. Therefore, after considering all these changes in the relative contribution, we conclude that for the 1st series of compound the energy transfer from Tb^{3+} ion at Ca2 site to Eu^{3+} ion at Ca1 site (Tb^{3+}@Ca2 → Eu^{3+}@Ca1) is the dominant one. Interestingly, for the 2nd series of compounds wherein the concentration of Tb^{3+} ion is fixed, we have not observed much difference in the respective contribution of two different Eu^{3+} components and for the higher concentration of Eu^{3+} in compound like $Eu_{0.5}$–$Tb_{0.5}$:CFP, the percentage is a bit higher for the long-lived Eu^{3+} component. Therefore, we may conclude that for the 2nd series of compounds, the energy transfer process from the excited Tb^{3+} ion at Ca1 site to Eu^{3+} ions at both Ca1 and Ca2

sites (Tb^{3+}@Ca1 → Eu^{3+}@Ca1 and Tb^{3+}@Ca1 → Eu^{3+}@Ca2) is happening with a bit more preference towards the Eu^{3+} ion at Ca2 site (Tb^{3+}@Ca1 → Eu^{3+}@Ca2).

4 Conclusion

Various Eu^{3+} and Tb^{3+} co-doped $Ca_{10}(PO_4)_6F_2$ compounds were synthesized by solid-state reaction method. Photoluminescence study showed that with varying the concentration of Tb^{3+} and Eu^{3+} ions, the colour characteristics can be tuned from yellow to orange to red. We have found that there is an energy transfer process involved from Tb^{3+} ion to Eu^{3+}, which is responsible for the tunable emission characteristics and the decay kinetics. It was observed that two different lifetime components exist for both Eu^{3+} and Tb^{3+} ions depending on their distribution among the two different Ca-sites (Ca1 in CaO_9 and Ca2 in CaO_6F network). The long-lived component for both the dopant ions are attributed to Ca2 site in CaO_6F network, wherein the F atom made the difference in lifetime of the excited state due to less quenching effect compared to O-atom. From density functional theory (DFT) based calculations we have observed that Tb^{3+} ions prefer to go to the Ca2 site while Eu^{3+} ions prefer the Ca site, when they are co-doped in $Ca_{10}(PO_4)_6F_2$ in a structure associated Ca vacancy. This site specific distribution was found to influence the energy transfer dynamics. It has been observed from the lifetime study that for the 1st series of compounds, wherein the concentration Tb^{3+} ions are fixed, the energy transfer Tb^{3+}@Ca2 → Eu^{3+}@Ca1 energy transfer is more preferable than Tb^{3+}@Ca1 → Eu^{3+}@Ca2. However, for the 2nd series of compounds, wherein the concentration Eu^{3+} ions are fixed, both the energy transfer processes Tb^{3+}@Ca1 → Eu^{3+}@Ca1 and Tb^{3+}@Ca1 → Eu^{3+}@Ca2 were involved with a bit more preference for Tb^{3+}@Ca1 → Eu^{3+}@Ca2.

Author contributions

Nimai Pathak: conceptualization, methodology, supervision, visualization, photoluminescence investigation, data analysis of all the experiments, writing-initial draft, reviewing and editing.

Bhagyalaxmi Chundawat: preparation of all the compound and XRD measurement.

Pratik Das: helping in preparation of compounds and FTIR measurement.

Pampa Modak: writing and helping in the theoretical study.

Brindaban Modak: VASP simulation and theoretical data analysis.

Conflicts of interest

There are no conflicts to declare.

Acknowledgements

References

1 Q. Zhou, L. Dolgov, A. M. Srivastava, L. Zhou, Z. Wang, J. Shi, M. D. Dramićanin, M. G. Brik and M. Wu, *J. Mater. Chem. C*, 2018, **6**, 2652–2671.

2 M. Xin, D. Tu, H. Zhu, W. Luo, Z. Liu, P. Huang, R. Li, Y. Cao and X. Chen, *J. Mater. Chem. C*, 2015, **3**, 7286–7293.

3 E. F. Schubert and J. K. Kim, *Science*, 2005, **308**, 1274–1278.

4 A. A. Setlur, W. J. Heward, Y. Gao, A. M. Srivastava, R. G. Chandran and M. V. Shankar, *Chem. Mater.*, 2006, **18**, 3314–3322.

5 N. Liu, L. Mei, L. Liao, J. Fu and D. Yang, *Sci. Rep.*, 2019, **9**, 15509.

6 G. Li, D. Geng, M. Shang, Y. Zhang, C. Peng, Z. Cheng and J. Lin, *J. Phys. Chem. C*, 2011, **115**, 21882–21892.

7 H. Liu, L. Liao, M. S. Molokeev, Q. Guo, Y. Zhang and L. Mei, *RSC Adv.*, 2016, **6**, 24577–24583.

8 (*a*) P. Das, N. Pathak, P. Modak and B. Modak, *J. Hazard. Mater.*, 2021, **411**, 125025; (*b*) N. Pathak, P. Das, B. Chundawat, P. Modak and B. Modak, *J. Hazard. Mater.*, 2021, **423**, 126980.

9 P. Das, N. Pathak, B. Sanyal, S. Dash and R. M. Kadam, *J. Alloys Compd.*, 2019, **810**, 151906.

10 S. Unithrattil, H. J. Kim, K. H. Gil, N. H. Vu, V. H. Hoang, Y. H. Kim, P. Arunkumar and W. B. Im, *Inorg. Chem.*, 2017, **56**, 5696–5703.

11 (*a*) S. K. Gupta, P. S. Ghosh, N. Pathak and R. M. Kadam, *RSC Adv.*, 2016, **6**, 42923–42932; (*b*) M. Sahu, N. Pathak and M. K. Saxena, *RSC Adv.*, 2021, **11**, 17488–17497.

12 X. Yan, G. R. Fern, R. Withnall and J. Silver, *Nanoscale*, 2013, **5**, 8640–8646.

13 P. Van Do, N. X. Ca, L. D. Thanh, N. Van Nghia and T. T. C. Thuy, *Phys. Chem. Chem. Phys.*, 2020, **22**, 27590–27599.

14 R. Mi, J. Chen, Y.-g. Liu, M. Fang, L. Mei, Z. Huang, B. Wang and C. Zhaob, *RSC Adv.*, 2016, **6**, 28887–28894.

15 Y. Gao, X. Sun, Z. Feng, L. Zhu, J. Zhang, W. Gao, X. Zhou, R. Cong and T. Yang, *New J. Chem.*, 2017, **41**, 2037–2045.

16 B. Zhang, H. Zou, H. Guan, Y. Dai, Y. Song, X. Zhou and Y. Sheng, *CrystEngComm*, 2016, **18**, 7620–7628.

17 M. Yang, Y. Liang, Q. Gui, B. Zhao, D. Jin, M. Lin, L. Yan, H. You, L. Dai and Y. Liu, *Sci. Rep.*, 2015, **5**, 11844.

18 G. Kresse and D. Joubert, *Phys. Rev. B: Condens. Matter Mater. Phys.*, 1999, **59**, 1758–1775.

19 P. E. Blöchl, *Phys. Rev. B: Condens. Matter Mater. Phys.*, 1994, **50**, 17953–17979.

20 J. P. Perdew, J. A. Chevary, S. H. Vosko, K. A. Jackson, M. R. Pederson, D. J. Singh and C. Fiolhais, *Phys. Rev. B: Condens. Matter Mater. Phys.*, 1992, **46**, 6671–6687.

21 J. P. Perdew, K. Burke and M. Ernzerhof, *Phys. Rev. Lett.*, 1996, **77**, 3865–3868.

22 H. J. Monkhorst and J. D. Pack, *Phys. Rev. B: Solid State*, 1976, **13**, 5188–5192.

23 J. Paier, M. Marsman, K. Hummer, G. Kresse, I. C. Gerber and J. G. Angyán, *J. Chem. Phys.*, 2006, **124**, 154709.

24 B. Modak and S. K. Ghosh, *Phys. Chem. Chem. Phys.*, 2018, **20**, 20078–20087.

25 V. Louis-Achille, L. De Windt and M. Defranceschi, *Comput. Mater. Sci.*, 1998, **10**, 346.

26 P. H. J. Mercier, Z. Dong, T. Baikie, Y. Le Page, T. J. White, P. S. Whitfield and L. D. Mitchel, *Acta Crystallogr.*, 2007, **63**, 37–48.

27 L. Calderín, M. J. Stott and A. Rubio, *Phys. Rev. B: Condens. Matter Mater. Phys.*, 2003, **67**, 134106.

28 P. Rulis, L. Z. Ouyang and W. Y. Ching, *Phys. Rev. B: Condens. Matter Mater. Phys.*, 2004, **70**, 155104.

29 C.-X. Li, Y.-H. Duan and W.-C. Hu, *J. Alloys Compd.*, 2015, **619**, 66–77.

30 Q. Zeng, H. Liang, G. Zhang, M. D. Birowosuto, Z. Tian, H. Lin, Y. Fu, P. Dorenbos and Q. Su, *J. Phys.: Condens. Matter*, 2006, **18**, 9549–9560.

31 P. Modak and B. Modak, *Phys. Chem. Chem. Phys.*, 2020, **22**, 16244–16257.

32 B. Modak, P. Modak and S. K. Ghosh, *J. Phys. Chem. C*, 2017, **121**, 12980–12990.

33 M. Sen, R. Shukla, N. Pathak, K. Bhattacharyya, V. Sathian, P. Chaudhury, M. S. Kulkarni and A. K. Tyagi, *Mater. Adv.*, 2021, **2**, 3405–3419.

34 (*a*) R. Phatak, N. Pathak, S. Muhammed, S. K. Sali and A. Das, *ChemPlusChem*, 2018, **83**, 1144–1152; (*b*) R. Phatak, N. Pathak, S. Muhammed, A. Das and S. K. Sali, *J. Am. Ceram. Soc.*, 2020, **103**, 2617–2629; (*c*) N. Pathak, S. Mukherjee, D. Das and D. Dutta, *J. Alloys Compd.*, 2021, **887**, 161414.

35 (*a*) N. Pathak, S. Mukherjee, B. P. Mandal, A. K. Yadav, S. N. Jha and D. Bhattacharyya, *Mater. Adv.*, 2020, **1**, 2380–2394; (*b*) N. Pathak, P. S. Ghosh, S. Mukherjee and B. P. Mandal, *RSC Adv.*, 2020, **10**, 31070–31086; (*c*) N. Pathak, S. Mukherjee, D. Das, D. Dutta, S. Dash and R. M. Kadam, *J. Mater. Chem. C*, 2020, **8**, 7149–7161; (*d*) S. Mukherjee, N. Pathak, D. Das and D. Dutta, *RSC Adv.*, 2021, **11**, 5815–5831; (*e*) D. Hebbar, K. S. Choudhari, N. Pathak, S. A. Shivashankar and S. D. Kulkarni, *J. Alloys Compd.*, 2018, **768**, 676–685; (*f*) K. Sanyal, N. Pathak, A. K. Yadav, B. Kanrar, R. M. Kadam, S. N. Jha, D. Bhattacharya and N. L. Misra, *Dalton Trans.*, 2016, **45**, 7650–7664; (*g*) S. K. Gupta, P. S. Ghosh, N. Pathak and R. M. Kadam, *RSC Adv.*, 2016, **6**, 42923–42932; (*h*) D. Hebbar, K. S. Choudhari, N. Pathak, S. A. Shivashankar and S. D. Kulkarni, *Mater. Res. Bull.*, 2019, **119**, 110544; (*i*) S. K. Gupta, N. Pathak and R. M. Kadam, *J. Lumin.*, 2016, **169**, 106–114; (*j*) S. K. Gupta, K. S. Prasad, N. Pathak and R. M. Kadam, *J. Mol. Struct.*, 2020, **1221**, 128776.

36 S. K. Gupta, N. Pathak, S. K. Thulasidas and V. Natarajan, *J. Lumin.*, 2016, **169**, 669–673.